

Nonlinear States of the Screw Dynamo

Wolfgang Dobler,* Anvar Shukurov,† and Axel Brandenburg‡

Department of Mathematics, University of Newcastle, Newcastle upon Tyne, NE1 7RU, U.K.

(Dated: March 7, 2019)

The self-excitation of magnetic field by a spiral Couette flow between two coaxial cylinders is considered. We solve numerically the fully nonlinear, three-dimensional MHD equations for magnetic Prandtl numbers P_m (ratio of kinematic viscosity to magnetic diffusivity) between 0.14 and 10 and kinematic and magnetic Reynolds numbers up to about 2000. In the initial stage of exponential field growth (kinematic dynamo regime), we find that the dynamo switches from one distinct regime to another as the radial width δr_B of the magnetic field distribution becomes smaller than the separation of the field maximum from the flow boundary. The saturation of magnetic field growth is due to a reduction in the velocity shear resulting mainly from the spatially averaged part of the Lorentz force, which agrees with an asymptotic result for the limit of $P_m \ll 1$. In the parameter regime considered, the magnetic energy decreases with kinematic Reynolds number as $Re^{-0.82}$, which is approximately as predicted by the nonlinear asymptotic theory ($\sim Re^{-1}$). However, when the velocity field is maintained by a volume force (rather than by viscous stress) the relation between magnetic energy and kinematic Reynolds is much weaker.

PACS numbers: 07.55.Db, 95.30.Qd, 98.58.Fd, 98.62.En

Keywords:

I. INTRODUCTION

The screw dynamo is a system where magnetic field is generated by the (laminar) flow of an electrically neutral, but conducting fluid with helical streamlines, i.e.

$$\mathbf{u} = (0, r\Omega, u_z) \quad (1)$$

in cylindrical polar coordinates (r, φ, z) , with Ω and u_z the angular and axial velocities, respectively. It is one of the simplest dynamo systems known and the most symmetric one in the sense that the flow can be steady and uniform in the azimuthal and axial directions. As first shown by Lortz [1, 2] and Ponomarenko [3], such a flow can generate magnetic fields via dynamo action, i.e., without any external electromotive forces. Since the magnetic Reynolds number required for magnetic field generation by the screw dynamo is relatively low, this type of flow has been used in a series of laboratory dynamo experiments in Riga, e.g. Refs. [4, 5] which have recently achieved magnetic field growth and saturation [6, 7]. There are further plans to perform a dynamo experiment based on a similar (but time-dependent) flow [8, 9]. Dynamo action of this type can occur in the cooling systems of fast breeder reactors [10]. A related successful dynamo experiment is the Karlsruhe liquid

sodium facility [11, 12], which involves an ensemble of spiral flows. Since the magnetic Reynolds numbers achievable in laboratory flows are never very high, it is important to understand quantitatively the excitation properties of the system and to predict measurable characteristics of the dynamo including the strength, location and time dependence of the magnetic field in the nonlinear regime.

Other possible sites for screw dynamo action are astrophysical jets [13] where a helical flow capable of dynamo action can arise from the axial ejection of plasma from a rotating accretion disc [14].

In the present paper, we explore nonlinear states of the screw dynamo in the spiral Couette flow of a viscous fluid between two coaxial cylinders. Both the screw dynamo itself and the flow are simple enough to allow detailed analysis of the nonlinear behavior — a rare feature among MHD dynamo systems. In particular, this allows one to assess many of the empirical and heuristic arguments often applied to more complicated dynamo systems, such as the relevance of the marginally stable linear solution for the description of nonlinear states, and to understand the nonlinear states in considerable detail.

The plan of the paper is as follows. We briefly review previous studies of the screw dynamo in Sect. II, and then describe our model in Sect. III. Our results are presented in Sect. IV A for the (kinematic) stage of exponential growth and in Sect. IV B for saturated, non-linear states. The results are summarized in Sect. V.

*Electronic address: Wolfgang.Dobler@ncl.ac.uk

†Electronic address: Anvar.Shukurov@ncl.ac.uk

‡Electronic address: brandenb@nordita.dk; also at: Nordita, Blegdamsvej 17, DK-2100 Copenhagen Ø, Denmark

II. THE SCREW DYNAMO

The kinematic behavior of the screw dynamo, including that in the spiral Couette flow, is well explored using both asymptotic analysis [15, 16, 17, 18, 19] and numerical modeling [20, 21, 22, 23]. A discussion of the screw dynamo in a broader context of slow dynamos was presented by Soward [24]; in Gilbert and Ponty [25] the idea of the screw dynamo was generalized to certain non-axisymmetric flows and in Ponty et al. [26] this approach was applied to hydrodynamically unstable Ekman layers and it was shown numerically that screw-type dynamos can operate in such layers.

Consider a time-independent velocity field (1) where both the angular and axial velocity are functions of cylindrical radius alone, $\Omega = \Omega(r)$ and $u_z = u_z(r)$. The evolution of the magnetic field \mathbf{B} is governed by the induction equation

$$\frac{\partial \mathbf{B}}{\partial t} = \nabla \times (\mathbf{u} \times \mathbf{B} - \eta \nabla \times \mathbf{B}), \quad (2)$$

where η is the magnetic diffusivity. At the kinematic stage, when the magnetic field is weak enough, \mathbf{u} can be considered fixed and independent of \mathbf{B} . The magnetic field can then grow exponentially provided the magnetic Reynolds number is above a certain critical value, and Eq. (2) becomes an eigenvalue problem. The field is necessarily non-axisymmetric (in accordance with Cowling's theorem, e.g. Ref. [27]) and, due to the symmetry of the flow, is a superposition of eigenmodes given in cylindrical polar coordinates by

$$B_j(r, \varphi, z, t) = \hat{B}_j(r) e^{i(m\varphi + kz) + \lambda t}, \quad j = r, \varphi, z, \quad (3)$$

where m and k are the azimuthal and axial wavenumbers, respectively, and

$$\lambda = \gamma + i\omega$$

is the eigenvalue, with γ the growth rate and ω the oscillation frequency of the magnetic field.

While Ponomarenko [3] discussed a rigid cylinder moving in a conducting medium — thus giving rise to a discontinuous velocity profile — later models [15, 16, 24] apply to more realistic, continuous velocity fields like the spiral Couette–Poiseuille flow, of which the spiral Couette flow used in the present paper is a special case.

The coupling of the radial and azimuthal components of Eq. (2), required for the magnetic field to grow ($\gamma > 0$), occurs via the diffusion term and is thus proportional to η — see Eqs. (A1) and (A2). Therefore, the growth rate of any given magnetic eigenmode (i.e., for fixed m and k) tends to zero as $\eta \rightarrow 0$. The scaling of the growth rate with the magnetic Reynolds number $R_m \propto \eta^{-1}$ depends on the flow properties. In the asymptotic limit $R_m \gg 1$, $\gamma = \mathcal{O}(R_m^{-1/2})$ for a continuous velocity field [15], whereas $\gamma = \mathcal{O}(R_m^{-1/3})$ for a discontinuous velocity field [3, 28]. The eigenfunction has a maximum at a

radius r_0 where the advection term $m\Omega(r) + ku_z(r)$ [see Eqs. (A1) and (A2) in Appendix A] has an extremum in r , thus minimizing destruction of the magnetic structure by the r -dependent advection. This implies that r_0 satisfies

$$m\Omega'(r_0) + ku_z'(r_0) = 0, \quad (4)$$

where primes denote the derivative with respect to r . (In a discontinuous flow, the eigenfunction is localized at the discontinuity.) Modes with different ratios k/m are localized at different radii. Growing modes can only exist if the condition [16]

$$\left| \frac{d \ln |\Omega' / u_z'|}{d \ln r} \right| < 4 \quad (5)$$

is satisfied at $r = r_0$, which is always the case for the spiral Couette flow.

The oscillation frequency of a mode localized at $r = r_0$ is given by

$$\omega = -m\Omega(r_0) - ku_z(r_0) + \mathcal{O}(R_m^{-1/2})$$

for a continuous flow with $m, k = \mathcal{O}(1)$.

The critical magnetic Reynolds number $R_m^{(\text{cr})}$, above which $\gamma > 0$, depends on the radial velocity profile and is about 20 or larger [4, 5, 20, 23]. The field concentrates in a cylindrical shell of width $\delta r = \mathcal{O}(R_m^{-1/4})$ (for $R_m \gg 1$) for a continuous velocity field [15] and $\delta r = \mathcal{O}(R_m^{-1/3})$ for a discontinuous velocity profile [3], provided $m, k = \mathcal{O}(1)$. At distances from r_0 larger than δr , advective distortion of the nonaxisymmetric magnetic field cannot be balanced by local dynamo action. Therefore the magnetic field must be weaker than in the resonance shell around r_0 and decays exponentially in $(r - r_0)^2$. Gilbert [16] has obtained asymptotic solutions for the fastest mode, $m, k = \mathcal{O}(R_m^{1/3})$ for continuous, and $m, k = \mathcal{O}(R_m^{1/2})$ for discontinuous velocity fields.

The nonlinear behavior of the screw dynamo has been studied only recently in a paper by Bassom and Gilbert [29], who have carried out an asymptotic analysis of the nonlinear case in the limit $\text{Re} \gg R_m \gg 1$, where Re is the kinematic Reynolds number. This implies a small magnetic Prandtl number, $P_m \equiv R_m/\text{Re} \ll 1$. The basic idea of their approach is that the overall effect of the magnetic field on the flow is dominated by the azimuthally and vertically averaged Lorentz force. The exponential growth of the kinematic stage is saturated via a reduction in the velocity shear in the vicinity of $r = r_0$ where dynamo action is most efficient. In the asymptotic limit considered, the velocity shear is fully suppressed (to a given asymptotic order) by magnetic forces in a shell of a radial width $\sim \mathcal{O}(R_m^{-1/10})$. Outside the shell, where the magnetic field is weaker, magnetic diffusion and stretching balance each other to maintain the magnetic field against Ohmic decay. At still larger distances from r_0 , shear dominates and the magnetic field is weak as at the

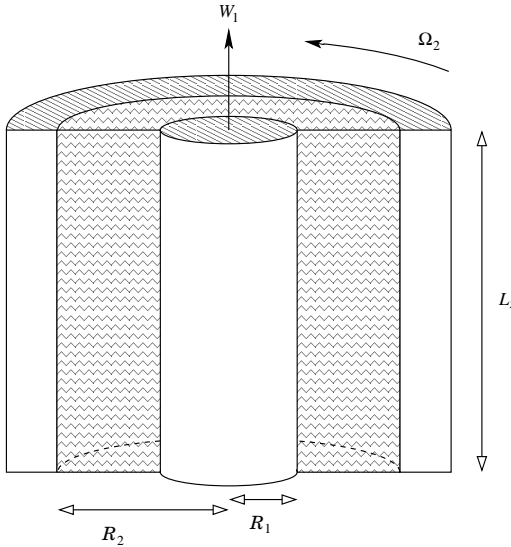


FIG. 1: The geometrical configuration of the simulations. The outer cylinder rotates at angular velocity Ω_2 , while the inner cylinder moves in the axial direction at speed W_1 .

kinematic stage. The steady-state field strength B_{ss} in the spiral Couette flow is estimated as [29]

$$\frac{B_{ss}^2}{\mu_0 \varrho U^2} = \mathcal{O}(R_m^{2/5} \text{Re}^{-1}), \quad (6)$$

where U is a characteristic value of the velocity and μ_0 the magnetic permeability. As we argue below, the scaling with Re is sensitive to the nature of the driving force and arises in Eq. (6) because the flow is driven by viscous forces.

III. THE MODEL

A. The spiral Couette flow

The geometry of our model is shown in Fig. 1. The conducting fluid is confined in the gap $R_1 < r < R_2$ between two coaxial cylinders that move with axial velocities W_1 and W_2 and rotate with angular velocities Ω_1 and Ω_2 , respectively. We choose $\Omega_1 = W_2 = 0$; the resulting flow then trivially satisfies Rayleigh's stability criterion, $\Omega_2 R_2^2 > \Omega_1 R_1^2$ [30]. The magneto-rotational instability of the Couette flow is discussed in Refs. [31, 32, 33]; our flow is stable with respect to this instability because $d\Omega/dr > 0$.

In the absence of a magnetic field, viscosity causes the fluid between the cylinders to adjust itself to the spiral Couette velocity profile

$$\Omega^{(C)} = C_1 \left(1 - \frac{R_1^2}{r^2} \right), \quad u_z^{(C)} = C_2 \ln \frac{R_2}{r}, \quad (7)$$

where

$$C_1 = \frac{\Omega_2 R_2^2}{R_2^2 - R_1^2}, \quad C_2 = \frac{W_1}{\ln(R_2/R_1)}.$$

The velocity profile (7), driven by the viscous stress, adjusts itself over the viscous relaxation time,

$$\tau_{\text{visc}} \approx \frac{(R_2 - R_1)^2}{\pi^2 \nu}, \quad (8)$$

which is in the range 1–80 for the models discussed below and is normally shorter than the time scale of magnetic field evolution.

B. Basic equations

The equations we solve are the MHD equations for the vector potential \mathbf{A} , the velocity \mathbf{u} and the density ϱ :

$$\frac{\partial \mathbf{A}}{\partial t} = \mathbf{u} \times \mathbf{B} + \eta \Delta \mathbf{A} + (\nabla \cdot \mathbf{A}) \nabla \eta, \quad (9)$$

$$\frac{D \mathbf{u}}{D t} = -\frac{1}{\varrho} \nabla p + \frac{\mu}{\varrho} (\Delta \mathbf{u} + \frac{1}{3} \nabla \nabla \cdot \mathbf{u}) + \frac{\mathbf{j} \times \mathbf{B}}{\varrho}, \quad (10)$$

$$\frac{D \varrho}{D t} = -\varrho \nabla \cdot \mathbf{u}, \quad (11)$$

complemented by an isothermal equation of state, $p = c_s^2 \varrho$, with constant speed of sound c_s . Here, the magnetic flux density \mathbf{B} and electric current density \mathbf{j} are given by $\mathbf{B} = \nabla \times \mathbf{A}$, $\mu_0 \mathbf{j} = \nabla \times \mathbf{B}$; $D/Dt \equiv \partial/\partial t + (\mathbf{u} \cdot \nabla)$ is the advective derivative, and μ is the dynamical viscosity (assumed constant). Below we refer to the Reynolds number based on the average kinematic viscosity, $\nu = \mu/\overline{\varrho}$.

We use an explicit finite-difference scheme of sixth order in space and third order in time described, e.g., in Ref. [34]. The velocity field outside the fluid shell, i.e. for $r < R_1$ and $r > R_2$, is prescribed and fixed, with $\mathbf{u} = (0, 0, W_1)$ in $r < R_1$ and $\mathbf{u} = (0, \Omega_2 r, 0)$ in $r > R_2$. We embed the cylinders into a Cartesian box and solve Eqs. (9)–(11) on a Cartesian mesh in order to avoid a coordinate singularity on the axis and to retain the applicability of the code to a range of geometries.

We assume the magnetic diffusivity η to be constant for $r < R_2 - 3\delta x$ (with δx the mesh size), i.e. the inner cylinder has the same electric conductivity as the fluid, but η smoothly decreases to zero in $R_2 - 3\delta x < r < R_2$. Thus, the last term in Eq. (9) is only relevant close to the outer boundary of the fluid.

The outer cylinder is assumed to be magnetically impenetrable, which confines the magnetic field to the region $r < R_2$. This would best be achieved with a perfect conductor at $r \geq R_2$, but this corresponds to an infinite magnetic Reynolds number, the numerical implementation of which leads to fundamental difficulties. Therefore we use the stronger requirement $\mathbf{A} = \mathbf{0}$ for $r \geq R_2$ instead. We demonstrate in Sect. IV A that our results are

TABLE I: Parameters of the numerical simulations discussed in the text. For all runs, $R_1 = 0.3$, $R_2 = 1.2$, $L_z = 4$, $\Omega_1 = 0$, and $W_2 = 0$. The values of W_1 , Ω_2 , ν and η different from those of Model 1a are highlighted with bold face. The mesh has equal spacings in all three dimensions, $\delta x = \delta y = \delta z$ in all models except Model 1i where $\delta y = \delta x = \delta z/2$.

Model	W_1	Ω_2	ν	η	U	U_{\max}	Re	R_m	P_m	δx
1a	1.0	1.3	2×10^{-2}	7×10^{-3}	1.85	1.56	111	318	2.9	0.033
1b	1.0	1.3	7×10^{-2}	7×10^{-3}	1.85	1.55	31.8	318	10	0.067
1c	1.0	1.3	1×10^{-2}	7×10^{-3}	1.85	1.55	222	318	1.4	0.067
1d	1.0	1.3	2.5×10^{-3}	7×10^{-3}	1.85	1.55	889	318	3.6	0.033
1e	1.0	1.3	1×10^{-3}	7×10^{-3}	1.85	1.55	2220	318	0.14	0.017
1f	1.0	1.3	2×10^{-2}	8×10^{-3}	1.85	1.55	111	278	2.5	0.067
1g	1.0	1.3	2×10^{-2}	4×10^{-3}	1.85	1.55	111	555	5.0	0.067
1h	1.0	1.3	2×10^{-2}	2×10^{-3}	1.85	1.56	111	1110	10	0.033
1i	1.0	1.3	2×10^{-2}	1×10^{-3}	1.85	1.56	111	2220	20	0.017
2a	0.5	1.3	2×10^{-2}	4×10^{-3}	1.64	1.55	98	491	5.0	0.033
2b	0.5	1.3	1×10^{-2}	4×10^{-3}	1.64	1.55	197	491	2.5	0.067
2c	0.5	1.3	7×10^{-2}	4×10^{-3}	1.64	1.55	197	491	18	0.067
2d	0.5	1.3	2×10^{-2}	2×10^{-3}	1.64	1.55	98	984	10	0.033

consistent with those obtained with a perfectly conducting outer cylinder since the magnetic field tends to concentrate close to the inner radius R_1 and thus the outer boundary condition only weakly affects the solution. We have counter-checked our results with a modified magnetic condition, where the vector potential is ‘softly’ set to zero in the region $r > R_2$ by means of an additional relaxation term $-\mathbf{A}/\tau_{\mathbf{A}}$ in the induction equation (9), and we only report results that are not qualitatively affected by this change.

We assume periodic boundary conditions in all three directions, imposed on the faces of the computational box. The horizontal boundary conditions are not actually important, since both the fluid and the magnetic field are confined to $r < R_2$. In the axial direction (the z -direction), the assumption of periodicity introduces a maximum wavelength L_z (the vertical size of the box) and leads to a quantization of the vertical wavenumber k to

$$k_n = 2\pi n/L_z, \quad (12)$$

with integer n , for solutions that are harmonic in z . In this article, we only present simulations for one fixed value of L_z to ensure comparability of the different models.

Figure 2 shows how the quantization of k due to the finite value of L_z affects the dynamo system. We show the dependence of the kinematic growth rate γ on the continuous wave number k — obtained by solving the eigenvalue problem (A1)–(A2) as described in Sect. IV A) — and indicate the quantized values k_n which occur in our simulations. While the maximum growth rate can be up to 40% larger than the maximum rate measured at k_n (Model 1d), the optimal values of k are hardly lower than k_1 . Thus, our choice of L_z does not impose unrealistically small vertical scales on the magnetic field; still it would be desirable (but numerically more demanding) to, say, double L_z .

Equations (9)–(11) are written for compressible fluids, but our choice of parameters makes compressibility insignificant since the speed of sound is a factor of two larger than the maximum fluid velocity, which results in a density contrast of $\leq 12\%$. Equation (9) implies the gauge

$$\eta \nabla \cdot \mathbf{A} + \Phi = 0, \quad (13)$$

where Φ is the electrostatic potential, related to the electric field \mathbf{E} by $\mathbf{E} = -\nabla\Phi - \partial\mathbf{A}/\partial t$. This gauge has proved to be most convenient for numerical purposes.

C. Parameters

The kinematic and magnetic Reynolds numbers are defined as

$$\text{Re} = UR_2/\nu, \quad R_m = UR_2/\eta, \quad (14)$$

where $U = \sqrt{(R_2\Omega_2)^2 + W_1^2}$ is a characteristic velocity. Their ratio is the magnetic Prandtl number

$$P_m = R_m/\text{Re}. \quad (15)$$

The parameter range investigated here is indicated in Table I. Parameters that remain constant for all the simulations are the cylinder radii ($R_1 = 0.3$ and $R_2 = 1.2$), and the size of the computational box: $L_z = 4$ for the vertical size and $L_x = L_y = 2(R_2 + 3\delta x)$ for the horizontal dimensions. The numerical resolution is either $42 \times 42 \times 60$ (corresponding to $\delta x \approx 0.067$) or $78 \times 78 \times 120$ grid points ($\delta x \approx 0.033$) except for Model 1i where the resolution is $144 \times 144 \times 120$ ($\delta x \approx 0.017$).

Models 1 and 2 differ in the values of W_1 and Ω_2 and have therefore distinct velocity profiles. This results in different dynamo efficiencies; for example, $R_m^{(\text{cr})} = 218$ in Model 1 and $R_m^{(\text{cr})} = 384$ in Model 2. Another important

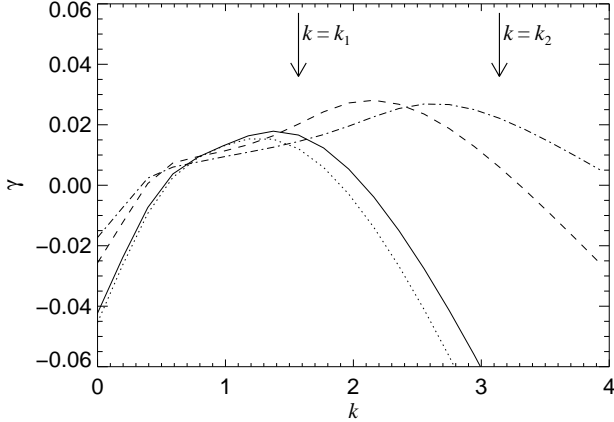


FIG. 2: Kinematic growth rate γ versus vertical wave number k for Models 1f (· · ·), 1a (—), 1d (— · —), and 1e (— · · —). The first two wave numbers k_1, k_2 allowed by $L_z = 4$ are indicated by vertical arrows.

distinction is the position of the magnetic field maximum, r_0 : in Model 1, the magnetic field is localized closer to the inner cylinder than in Model 2 (see e.g. the insets in Fig. 3 and 4 or Fig. 12 in Appendix B). The models are further subdivided (1a–f, 2a–d) according to the values of ν and η in order to explore the effects of varying magnetic and kinematic Reynolds numbers. Most of our models have $P_m > 1$, except Model 1d ($P_m \approx 0.36$) and Model 1e ($P_m = 0.14$).

IV. RESULTS

A. Kinematic regime

The velocity profile (7) can be considered as fixed, and Eq. (2) as linear in \mathbf{B} , as long as the magnetic stress is weak compared to the viscous stress,

$$\frac{B^2}{\mu_0} \ll \rho\nu \frac{U}{R_2 - R_1}. \quad (16)$$

Equations for the resulting kinematic dynamo problem are given in Appendix A. As discussed in Sect. II, they represent a one-dimensional eigenvalue problem which is relatively straightforward to solve numerically. For Models 1 and 2 we show in Figs. 3 and 4 the dependence of the growth rate γ and frequency ω on the magnetic Reynolds number (solid lines) and compare them to the asymptotic formulae, which are given in Ref. [18] and are also reproduced in Appendix A (dashed lines in Figs. 3 and 4). The insets show the radial profile of magnetic energy for two values of R_m . The critical magnetic Reynolds number is $R_m^{(cr)} = 217.8$ for Model 1 and $R_m^{(cr)} = 383.7$ for Model 2.

The growth rate γ becomes positive at $R_m = R_m^{(cr)}$, first quickly increases with R_m , and then decreases as expected for a slow dynamo [24, 28]. For the continuous velocity profile (7), the analytic theory predicts an asymptotic

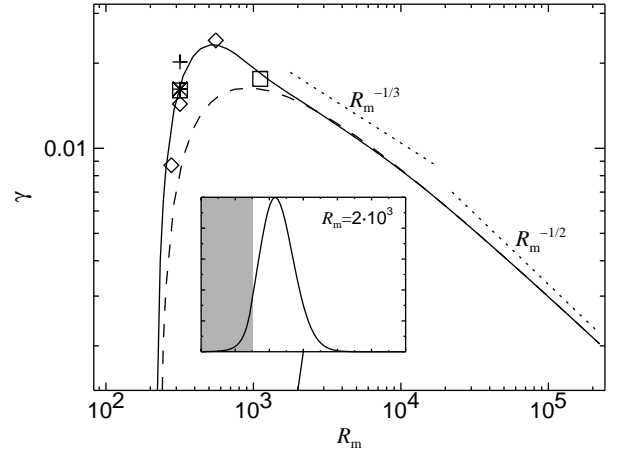


FIG. 3: Kinematic growth rate γ and frequency ω in Model 1 for the mode $m = 1$, $k = \pi/2$ (the dominant mode) as a function of the magnetic Reynolds number, obtained from the one-dimensional eigenvalue problem described in Sect. IV A. Dotted lines show the dependencies $\gamma \propto R_m^{-1/3}$ and $\gamma \propto R_m^{-1/2}$ in the upper panel and $(\omega - \text{const}) \propto R_m^{-1/2}$ in the lower panel. The asymptotic solution given in Appendix A is shown dashed. Results from the three-dimensional simulations are labeled according to the grid spacing: $\delta x = 0.13$ (+), 0.067 (\diamond), 0.033 (\square), and 0.017 (*). The insets show radial magnetic energy profiles in the domain $0 < r < R_2$ for $R_m = 2 \times 10^3$ (top) and $R_m = 2 \times 10^5$ (bottom); the region occupied by the inner cylinder is shaded. The generation threshold for this configuration is $R_m^{(cr)} \approx 218$.

decrease $\gamma \propto R_m^{-1/2}$ (Appendix A), and this scaling is indeed reached for very large values of R_m . However, while the growth rate for Model 2 (Fig. 4) agrees well with the asymptotic result (dashed), the agreement is not so good for $R_m \lesssim 2000$ in Model 1 (Fig. 3). Moreover, the latter model shows an approximate transient scaling $\gamma \sim R_m^{-1/3}$. Incidentally, this scaling is close to that for a flow with discontinuous radial profile [3, 16].

The difference can be explained as follows. For moderate magnetic Reynolds numbers, the field has noticeable strength at the boundary of the inner cylinder in the flow

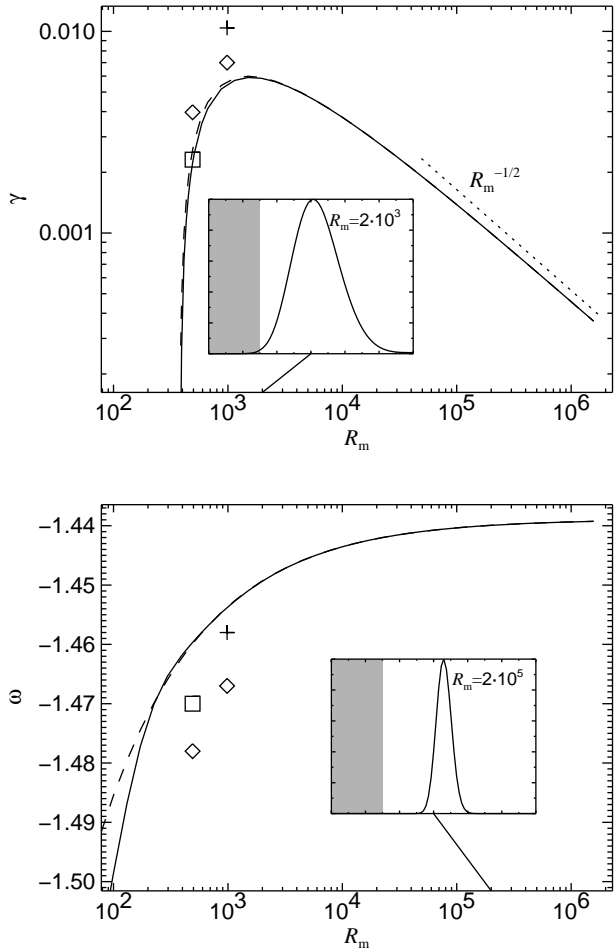


FIG. 4: As in Fig. 3, but for Model 2. The critical magnetic Reynolds number is $R_m^{(\text{cr})} \approx 384$.

of Model 1 (see inset in the top frame of Fig. 3). Therefore, the asymptotic theory is inapplicable as it is based on the assumption that the magnetic field is concentrated far from the boundaries $r = R_1$ and $r = R_2$. However, the radial width of the field distribution decreases with R_m and eventually the field at $r = R_1$ becomes negligible (see inset in the bottom frame of Fig. 3), and the scaling $\gamma \sim R_m^{-1/2}$ is recovered. On the other hand, the field is always small near the boundaries in Model 2 (see insets in Fig. 4), and so the scaling $\gamma \sim R_m^{-1/3}$ does not occur.

We have also explored the linear stage of magnetic field evolution using the three-dimensional code in order to assess its performance. A discussion of the numerical aspects is given in Appendix B. We start the simulations with a weak random magnetic field. After the initial transients have died away, exponential growth of magnetic energy is established, corresponding to the fastest growing mode.

Figure 5a shows the magnetic field structure for Model 1h. The level surfaces of $|\mathbf{B}|$ have the form of two helical flux tubes of opposite field orientation, which corresponds to an azimuthal wavenumber $m = 1$. The ver-

tical wavenumber of the solution shown is $k = 2\pi/L_z = \pi/2$. This mode is excited in all the models of Table I. However, higher modes are also excited in Models 1h, 1i, and 2d, where R_m is larger (see Table II).

Both the flow and the magnetic field are strongly helical, the two helicities being of opposite sign (the streamlines are right-handed spirals, while the magnetic field lines form left-handed helices as can be seen in Fig. 5). Since the screw dynamo mechanism relies on diffusion, the approximate conservation of magnetic helicity in highly conducting media, which leads to serious difficulties in mean-field dynamo theory [35, 36], does not lead to any problem here.

B. Nonlinear Simulations

After a phase of exponential growth, magnetic energy levels off at a certain saturation level. The corresponding magnetic energy density is comparable to (but smaller than) the kinetic energy density in the sheared flow, as can be seen from Table II, where we compare the maximum magnetic flux density to $\sqrt{\bar{\rho}U^2}$, and the magnetic energy to $E_{\text{kin}} = \frac{1}{2}\bar{\rho}U^2V$, where $V = L_z\pi(R_2^2 - R_1^2)$ is the fluid volume. The location and width of the magnetic energy maximum are characterized by

$$r_B = \langle r \rangle_{\mathbf{B}^2}, \quad \delta r_B = \langle (r - r_B)^2 \rangle_{\mathbf{B}^2}^{1/2}, \quad (17)$$

where $\langle f \rangle_{\mathbf{B}^2} = \int f \mathbf{B}^2 dV / \int \mathbf{B}^2 dV$ is the magnetic-energy weighted volume average. These quantities are similar to r_0 and δr of the kinematic theory.

1 The spatial structure of the magnetic field

Figure 6 shows the vertical profiles of the magnetic field in the saturated regime for various magnetic Reynolds numbers. The vertical component of the magnetic field is plotted as a function of z close to the radius where the field concentrates. Note that the antisymmetry of the curve with respect to the middle of the box indicates that only Fourier components with odd vertical wavenumbers are excited, which can be understood from the structure of the nonlinear terms in Eqs. (9)–(11). The profile in the saturated state is flattened in comparison to the (kinematic) eigenmode and this effect becomes more pronounced as R_m increases. The flattening of the maxima in both z and φ can also be seen in Fig. 5, where the level surface $|\mathbf{B}| = 0.65 |\mathbf{B}|_{\text{max}}$ is shown toward the end of the linear phase (Fig. 5a) and in the saturated state (Fig. 5b).

The strongly anharmonic profiles $B(z)$ found for large R_m do not occur in Bassom and Gilbert's [29] theory, which predicts harmonic profiles in the saturated state. The difference can be explained by the fact that here $P_m > 1$, whereas Bassom & Gilbert assume $P_m \ll 1$.

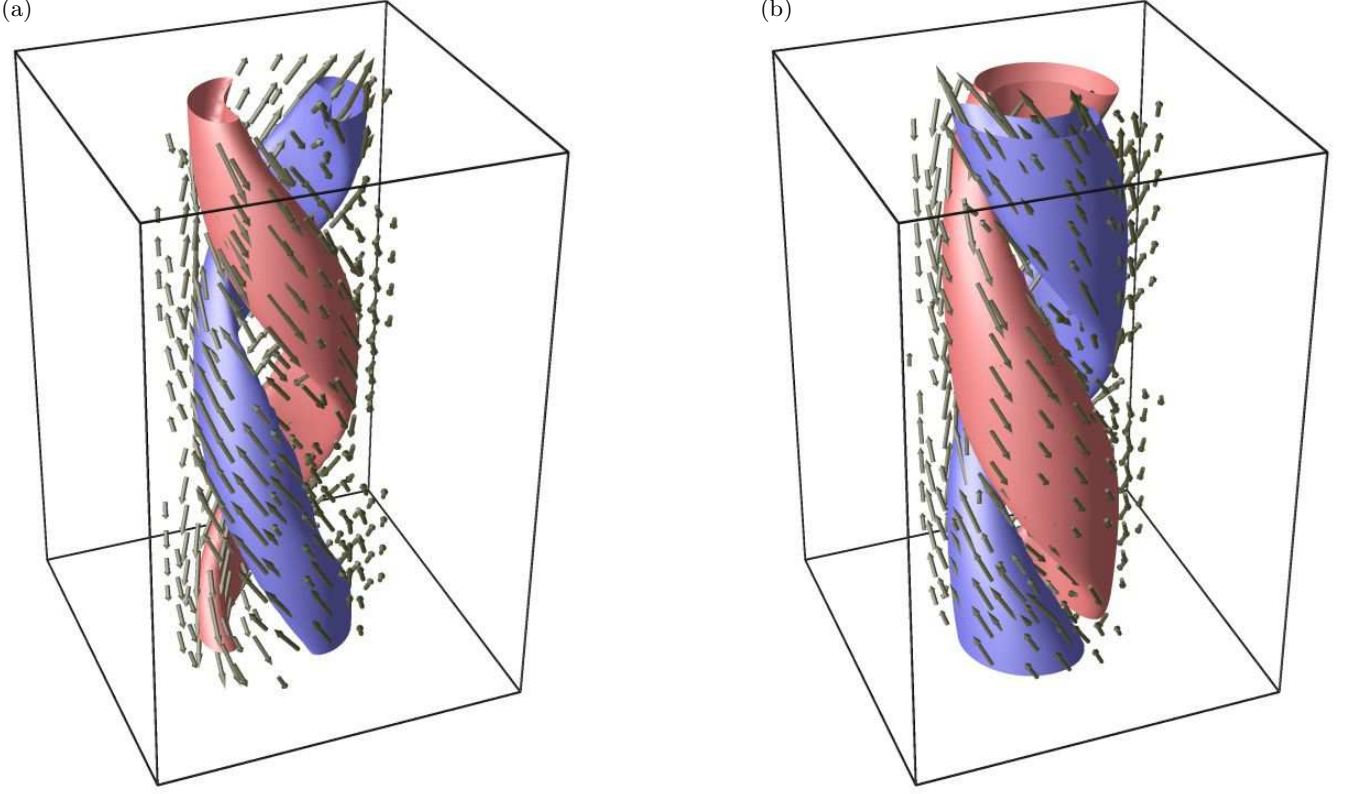


FIG. 5: Three-dimensional representation of the magnetic field in Model 1h. (a) $t = 200$ (end of the kinematic stage); (b) $t = 912$ (the saturated state). Shown are surfaces where $|\mathbf{B}|$ is 0.65 of the maximum and magnetic field vectors. The vertical component of the field has opposite sign in the two flux tubes shown (mode $m = 1$). The azimuthal and axial variations of the field are harmonic at the kinematic stage (a) and flattened in the saturated state (b) (see also Fig. 6).

TABLE II: Magnetic field properties in the models of Table I. Numbers in parentheses refer to the kinematic stage, all other quantities are for the saturated state. Shown are the growth rate γ and oscillation frequency ω of the leading mode; the maximum saturated magnetic field strength B_{\max} and magnetic energy E_{mag} in the flow region, both normalized to the corresponding kinetic quantities, and the position and width of the magnetic field distribution in radius, r_B and δr_B . The last column lists the growing modes in the form $(m, 2k/\pi)$, ordered by decreasing growth rate. The results for Models 1h, 1i, and 2d refer to the $(1, 1)$ mode only.

Model	γ	ω	$\frac{B_{\max}}{\sqrt{\rho U^2}}$	$\frac{E_{\text{mag}}}{E_{\text{kin}}}$	r_B	δr_B	$(m, 2k/\pi)$
1a	(0.0160)	-2.03 (-1.957)	0.33	0.015	0.49 (0.47)	0.17 (0.16)	(1, 1)
1b	(0.0144)	-2.014 (-1.957)	0.51	0.034	0.48 (0.47)	0.17 (0.16)	(1, 1)
1c	(0.0144)	-2.037 (-1.957)	0.24	0.008	0.48 (0.47)	0.17 (0.16)	(1, 1)
1d	(0.0144)	-2.045 (-1.957)	0.14	0.002	0.50 (0.47)	0.17 (0.16)	(1, 1)
1e	(0.0144)	-2.051 (-1.957)	0.08	0.0009	0.51 (0.47)	0.17 (0.17)	(1, 1)
1f	(0.0087)	-2.014 (-1.976)	0.25	0.008	0.48 (0.47)	0.17 (0.17)	(1, 1)
1g	(0.0232)	-2.028 (-1.935)	0.42	0.024	0.47 (0.47)	0.15 (0.14)	(1, 1)
1h	(0.0176)	-2.012 (-1.91)	0.47	0.030	0.47 (0.46)	0.13 (0.12)	(1, 1), (1, 2)
1i	(—)	-1.981 (—)	0.55	0.035	0.46 (—)	0.11 (—)	(1, 2), (1, 1), (2, 3), (2, 1), (2, 3)
2a	(0.0023)	-1.459 (-1.471)	0.17	0.006	0.63 (0.66)	0.18 (0.18)	(1, 1)
2b	(0.0039)	-1.459 (-1.473)	0.23	0.10	0.65 (0.67)	0.21 (0.20)	(1, 1)
2c	(0.0039)	-1.506 (-1.488)	0.48	0.41	0.63 (0.66)	0.20 (0.20)	(1, 1)
2d	(0.0071)	-1.506 (-1.467)	0.29	0.01	0.61 (0.66)	0.17 (0.17)	(1, 1), (1, 2)

The sensitivity of the solution to the value of the magnetic Prandtl number (if this is the true reason for the difference) is striking.

As can be seen in Fig. 7, the nonlinear distortion of the magnetic field distribution is only prominent in the azimuthal and axial profiles, but not much in the ra-

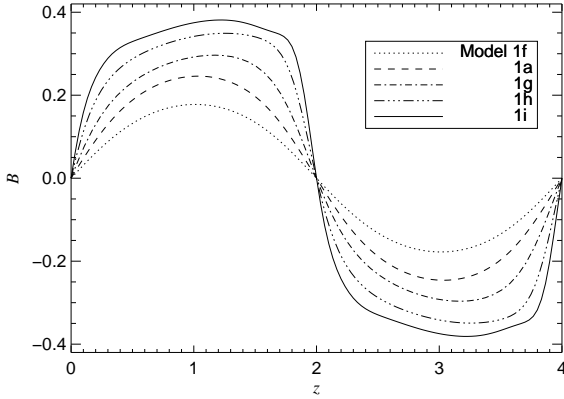


FIG. 6: Magnetic field structure in the saturation regime. Shown is, as a function of z , the vertical field B_z along a vertical line at $r = 0.48$ for Models 1f, 1a, 1g, 1h, and 1i; R_m grows monotonically along this sequence.

dial profile. We also note from Table II that in all the models the radial width of the magnetic energy distribution, δr_B , is in the nonlinear stage not significantly larger than in the kinematic stage. In Model 1i, for example, the radial width of the eigenfunction is, asymptotically, $\delta r = \mathcal{O}(R_m^{-1/3}) \simeq 0.1$ for a discontinuous velocity profile and $\delta r = \mathcal{O}(R_m^{-1/4}) \simeq 0.15$ for a smooth velocity. This should be compared with $\delta r_B \approx 0.11$ in the nonlinear regime. In all our simulations, the radial width of magnetic field distribution in both linear and nonlinear states is close to that predicted by the asymptotic theory for the kinematic dynamo. An equally good agreement of $\delta r_B \approx 0.19$ with the linear asymptotic result $\delta r \simeq R_m^{-1/4} = 0.18$ occurs also in Model 2d. This is at variance with the nonlinear asymptotics of Bassom and Gilbert [29] that predicts the development of a ‘core’ region in the radial profile of magnetic field with a width of order $\mathcal{O}(R_m^{-1/10}) \simeq 0.5$ in Model 1i. A plausible reason for this discrepancy with the nonlinear asymptotics might be that our models have too small values of R_m (2220 in Model 1i and 984 in Model 2d) for the asymptotic regime of Bassom & Gilbert to apply, even though the linear asymptotics are already accurate. It is more plausible, however, that solutions with moderate magnetic Prandtl number do not develop the $R_m^{-1/10}$ core and their radial profile is quite similar to that of the kinematic eigenfunction (see Fig. 7).

2 Nonlinear distortion of the velocity field

Figure 8 shows the radial velocity profiles for the saturated phase of Model 1a where the scatter of the data points is due to their different positions in φ and z . The radial velocity fluctuates around zero and is dynamically unimportant (even more so as perturbations in the ra-

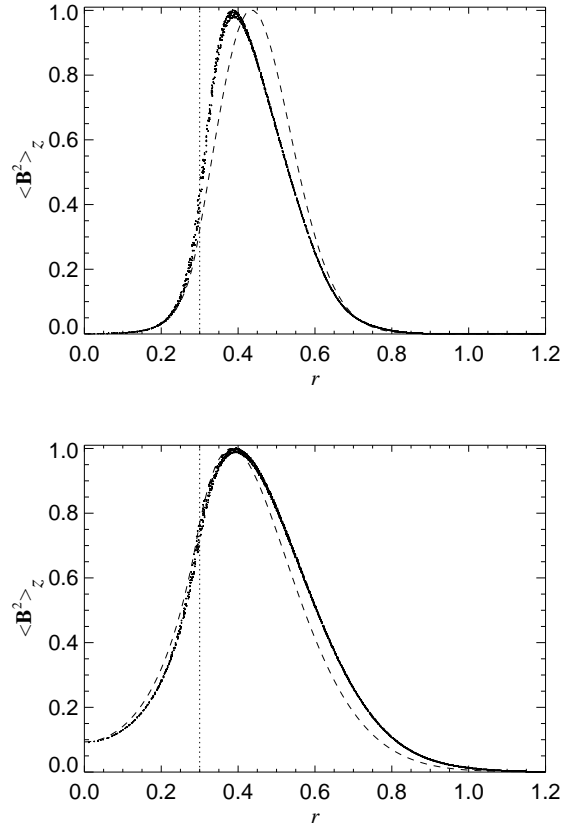


FIG. 7: The radial magnetic field profile in the saturated regime for Models 1i (top; $P_m = 20$), and 1e (bottom; $P_m = 0.14$). Shown is the vertically averaged magnetic energy density as a function of r (dots) and the corresponding profile at the kinematic dynamo stage (dashed), normalized to match the maximum of the nonlinear profile.

dial velocity can be balanced by the pressure gradient). However, the azimuthal and axial velocities exhibit systematic deviations from their Couette profiles so that the velocity shear is reduced in the region where the magnetic field concentrates. It is especially clear in the case of u_z (Fig. 8c) that the spatial scatter is smaller than the mean variation, so the distortion of the velocity field is axially symmetric and independent of z to a first approximation. To justify this we demonstrate in Fig. 11 that the radial profiles of the averaged Lorentz force are in close correspondence with the deviations of the respective velocity components of Fig. 8 from the Couette profile. This is compatible with the scenario of Bassom and Gilbert [29], where, in the limit of infinite kinematic and magnetic Reynolds numbers, the saturation of dynamo action is mainly due to the vertically and azimuthally averaged part of the Lorentz force. As the magnetic Reynolds number is increased, the relative distortion of the velocity field, and in particular the reduction of velocity shear, are getting more pronounced; this can be seen in Fig. 9, where we show the same profiles as in Fig. 8, but for a

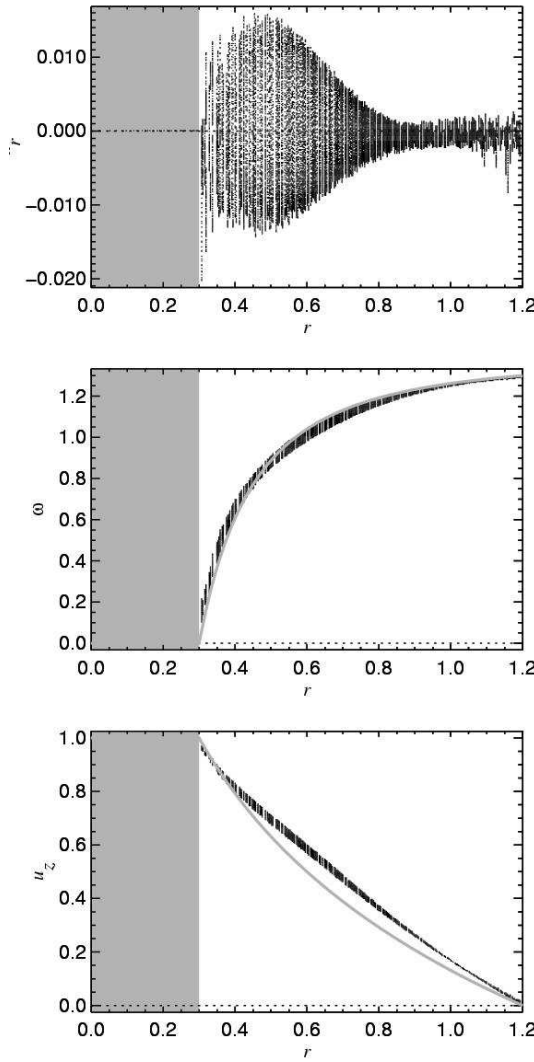


FIG. 8: The radial, azimuthal and vertical velocity components as functions of radius in the saturated stage for Model 1a at a resolution $\delta x = 0.033$. Note the different ranges on the ordinate in the panels: the variation of u_r is much smaller than that of $\omega(r)$ and $u_z(r)$. The shear in both $\omega(r)$ and $u_z(r)$ is reduced in comparison to that in the Couette profile $\mathbf{u}^{(C)}$ of Eq. (7), which is shown as a continuous gray line. The location of the inner cylinder is marked in gray. The scatter of the data points arises from their different positions in φ and z .

seven times larger value of R_m .

The radial width of the region where the velocity field is distorted away from the original Couette profile is much larger than that of the Lorentz force (see Fig. 11 below). This happens because the flow adjusts itself to two separate Couette profiles at both ends of the radial range where the Lorentz force has distorted it, and so a localized magnetic field does affect the flow throughout the domain. It can be expected that a flow profile driven by a volume force will be distorted less in regions where magnetic field is weak; our results confirm this expecta-

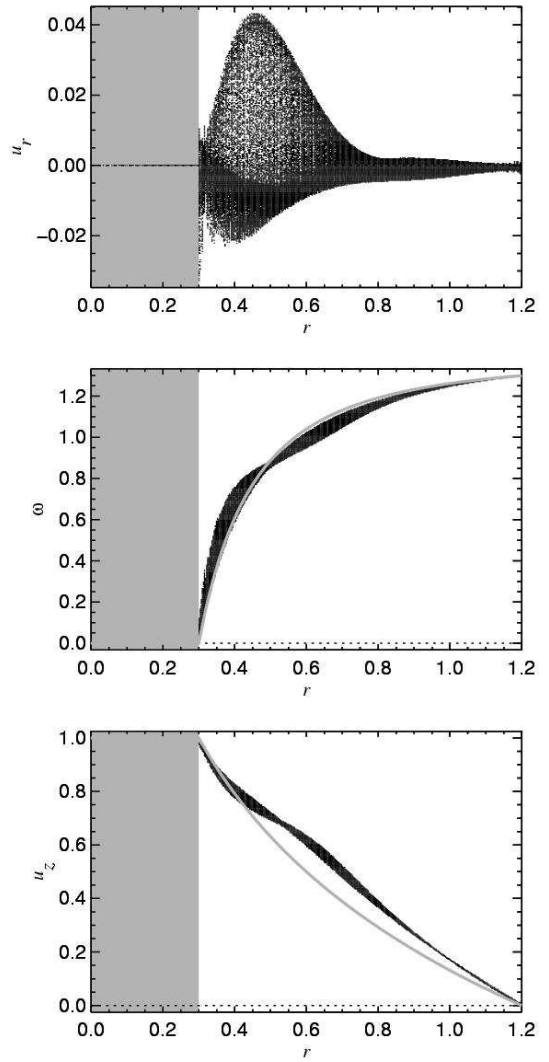


FIG. 9: As Fig. 8, but for Model 1i.

tion.

The screw dynamo can be interpreted in terms of the mean-field $\alpha\Omega$ -dynamo [24, 25], the ω - term being as usual the shear term $rB_r d\Omega/dr$ [see Eq. (A2)]. The α -effect is identified with a part of the diffusion term, and the corresponding term in the induction equation has the form

$$-\eta \frac{2}{r^2} \frac{\partial}{\partial \varphi} B_\varphi \quad (18)$$

[see Eq. (A1)]. Since the differential operator acting on B_φ is obviously not influenced by the magnetic field strength, the α -effect cannot be affected by the growing magnetic field and saturation is fully due to Ω -quenching. This is opposite to one of the standard scenarios for mean-field dynamos (α -quenching), where the magnetic field has little influence on the angular velocity and saturation is considered to be caused by the partial suppression of the α -effect by magnetic fields.

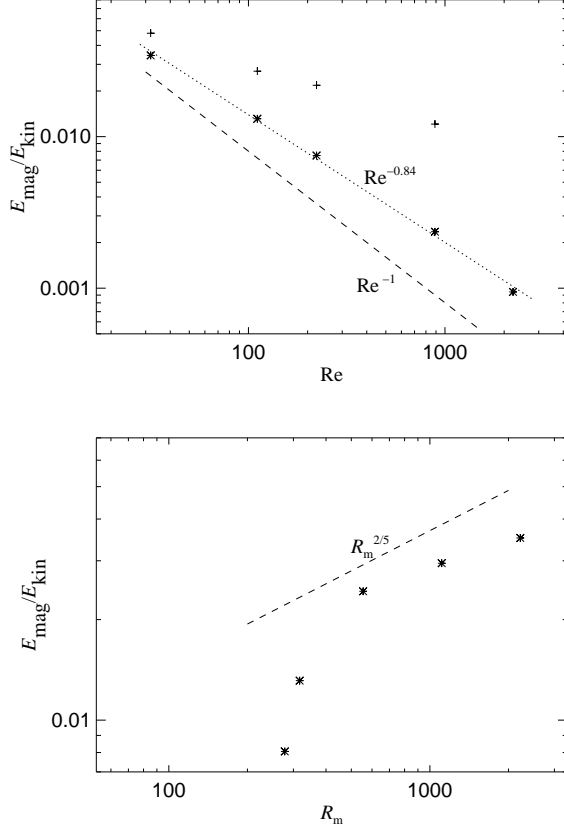


FIG. 10: Magnetic energy in the saturated state versus the kinematic and magnetic Reynolds numbers for Models 1a–i. Top: $E_{\text{mag}}/E_{\text{kin}}$ as a function of Re for Models 1b, 1a, 1c, 1d, and 1e (asterisks). The crosses refer to a model with volume forcing (see Sect. IV B 3). Bottom: $E_{\text{mag}}/E_{\text{kin}}$ as a function of R_m for Models 1f, 1a, 1g, 1h, and 1i. The dashed lines show the asymptotic power laws given in Eq. (6); the dotted line is a least-square power-law fit and corresponds to a dependence $E_{\text{mag}} \propto \text{Re}^{-0.84}$.

3 Magnetic energy scaling with Re and R_m

Figure 10 shows the magnetic energy in the saturated state as a function of the kinematic and magnetic Reynolds numbers. We also show the asymptotic scalings of Bassom and Gilbert [29]. There is clearly some agreement between the numerical and asymptotic results although the asymptotic solution has been obtained for $P_m \ll 1$ whereas the numerical results refer mostly to the case $P_m > 1$. We believe that the reason for the rough agreement is related to the fact that, in both cases, the magnetic feedback affects mainly the axisymmetric flow profile, as was seen in Fig. 8.

As expected (at least for weakly supercritical solutions) the steady-state magnetic field strength B_{ss} increases with magnetic Reynolds number. On the other hand, the saturated field strength B_{ss} decreases with Re in a flow driven by viscous stresses because it becomes

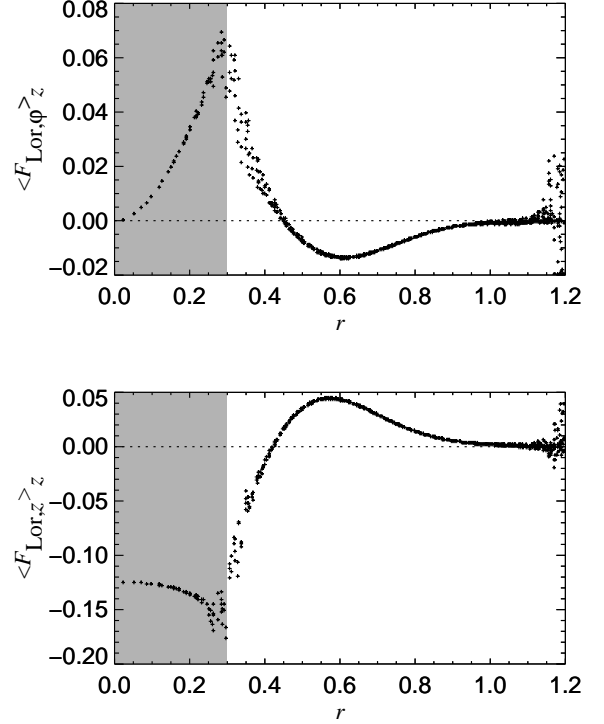


FIG. 11: Vertically averaged components of the Lorentz force as function of radius for Model 1a. Note that the effects of magnetic torques on the inner cylinder (shaded area in Fig. 11) are ignored in our model and its velocity remains fixed.

easier for the magnetic field to modify the velocity field in a given cylindrical shell as Re increases (owing to the weaker viscous coupling of fluid at different radii), and so weaker magnetic field is needed to achieve a local reduction in shear sufficient to halt the field growth. As we discuss below, this behavior is characteristic of a flow driven by viscous stresses but not by a volume force.

The scaling of magnetic energy with Re is slightly shallower than predicted by Bassom & Gilbert and has an exponent close to -0.82 rather than -1 . Similarly, the growth of magnetic energy with R_m is slower than $R_m^{2/5}$ at the values of R_m explored here. The most plausible reason for these disagreements is the difference in magnetic Prandtl numbers and, possibly, also the fact that the magnetic field distribution is still not narrow compared to the gap width $R_2 - R_1$ for the magnetic Reynolds numbers we were able to consider.

Taken at face value, the dependence of B_{ss} on Re discussed above implies that the resulting magnetic field will be negligible wherever $\text{Re} \gg 1$. However, in most real systems the flow will be driven by non-viscous forces. These are pressure and inertial forces in the dynamo experiments in Riga and Perm. In the case of astrophysical jets, acceleration and collimation of the flow can be due to an external magnetic field (axisymmetric to the

first approximation, then the screw dynamo can generate an additional nonaxisymmetric magnetic field). In these cases the kinematic Reynolds number will not play such a prominent role in the system and B_{ss} is expected to be independent of Re for $Re \gg 1$.

To justify this idea, we have carried out further numerical simulations for the parameters of Models 1b, 1a, 1c, and 1d, but with an additional volume force

$$-\frac{\mathbf{u} - \mathbf{u}^{(C)}}{\tau} \quad (19)$$

on the right-hand side of the equation of motion (10). Here $\mathbf{u}^{(C)}$ denotes the spiral Couette profile (7) and $\tau = 1.0$ is the time scale over which the flow adjusts itself to the Couette profile. With this choice of τ , we have $\tau < \tau_{visc}$, where τ_{visc} is the viscous time defined in Eq. (8). Thus, the Couette flow profile is now maintained on a dynamical time scale rather than by viscosity if $Re \gg 30$.

We show in Fig. 10 by crosses the resulting dependence of the steady-state magnetic energy on Re ; the dependence is clearly much weaker than in the case of viscous driving (a power-law fit to the points shown has an exponent of about -0.41). In the inviscid limit $Re \rightarrow \infty$ the magnetic energy must eventually become independent of viscosity, and so we anticipate that the dependence marked with crosses has a horizontal asymptote.

Another reason why the dependence (6) is not directly applicable to laboratory and astrophysical dynamo systems is that the corresponding flows are turbulent. In this case, the effective values of Re and R_m based on turbulent diffusivities will enter the solution, and these can be quite moderate. It can be expected, however, that turbulence in the Couette flow will be very inhomogeneous being generated mainly in turbulent boundary layers near the flow boundaries, and this can affect the theory discussed here. On the other hand, the reduction in the effective magnetic Reynolds number due to turbulence has to be only moderate since one needs $R_m \geq R_m^{(cr)}$ for any sort of dynamo action. Assuming that that turbulent magnetic and kinetic Reynolds numbers have similar orders of magnitude, $Re \simeq R_m$, and that $R_m^{(cr)} \simeq 10^2$, the resulting magnetic energy density will be about 10% of the kinetic energy density even with the scaling (6).

V. CONCLUSIONS

The numerical calculations performed here have revealed a new intermediate asymptotic regime in the kinematic screw dynamo where, in a certain range of R_m , the magnetic field eigenfunction is large enough at the flow boundary so that the standard asymptotic solutions are inapplicable and the growth rate of the magnetic field scales as $\gamma = \mathcal{O}(R_m^{-1/3})$. This dependence is typical of a discontinuous velocity profile. The standard asymptotic scaling, $\gamma = \mathcal{O}(R_m^{-1/2})$, is only recovered at significantly

larger values of R_m where the eigenfunction becomes narrow enough in radius as to satisfy the assumptions of the asymptotic theory.

We have confirmed the result of Bassom and Gilbert [29] that saturation of screw dynamo action occurs via a reduction in the velocity shear produced by the axisymmetric part of the Lorentz force. We have shown that this also applies to the case of large magnetic Prandtl numbers P_m . However, the radial profile of the nonlinear solution is very similar to the marginally stable eigenmode for the nonlinearly modified velocity field. This is different from the nonlinear asymptotics of Bassom and Gilbert, which predicts a plateau in the radial dependence. It is possible that such a plateau can only occur at values of the magnetic Prandtl number much smaller than we have been able to simulate in the present work, but we have not detected any tendency towards its development at $P_m = 014$, the smallest value explored here.

APPENDIX A: ONE-DIMENSIONAL, KINEMATIC DYNAMO PROBLEM

In cylindrical coordinates (r, φ, z) , the kinematic dynamo problem for given steady velocity field $(0, r\Omega(r), u_z(r))$, is given by the following non-dimensionalized set of equations for the two components B_r, B_φ

$$\lambda B_r + i(m\Omega + ku_z)B_r = \frac{1}{R_m} \left\{ \hat{D}B_r - \frac{2im}{r^2}B_\varphi \right\}, \quad (A1)$$

$$\begin{aligned} \lambda B_\varphi + i(m\Omega + ku_z)B_\varphi = & r \frac{d\Omega}{dr} B_r \\ & + \frac{1}{R_m} \left\{ \hat{D}B_\varphi + \frac{2im}{r^2}B_r \right\}, \end{aligned} \quad (A2)$$

where

$$\hat{D} = \frac{1}{r} \frac{d}{dr} \left(r \frac{d}{dr} \right) - \frac{m^2 + 1}{r^2} - k^2 \quad (A3)$$

is a self-adjoint, Laplace-type differential operator and λ is the eigenvalue. The vertical component B_z can be obtained from the solenoidality condition,

$$\frac{1}{r} \frac{d}{dr} (r B_r) + \frac{im}{r} B_\varphi + ik B_z = 0. \quad (A4)$$

For convenience, we give the expressions from second-order asymptotic analysis (for $R_m \rightarrow \infty$) for the spiral Couette flow as derived by [15, 18]. Generally, for a continuous velocity field $u_r = 0$, $u_\varphi = r\Omega(r)$, $u_z = u_z(r)$, the magnetic field concentrates around a radius r_0 which is a solution of Eq. (4). For spiral Couette flow, it is convenient to define a magnetic Reynolds number as

$$\tilde{R}_m = \frac{R_1^2 R_2^2}{R_2^2 - R_1^2} \frac{\Delta\Omega}{\eta} \equiv \frac{|\Omega'(r)|r^3}{\eta}; \quad (A5)$$

the radius r_0 is given by

$$r_0 = R_1 R_2 \sqrt{\frac{\ln R_2 - \ln R_1}{R_2^2 - R_1^2}} \sqrt{-2 \frac{m \Delta \Omega}{k \Delta W}} \quad (\text{A6})$$

and the field can only be growing if

$$\frac{m \Delta \Omega}{k \Delta W} < 0. \quad (\text{A7})$$

To second order in the small parameter $\tilde{R}_m^{-1/2}$, the (dimensional) eigenvalue λ is given by

$$\begin{aligned} \lambda + i[m\Omega(r_0) + ku_z(r_0)] \\ = \frac{\eta}{r_0^2} \left\{ (\sqrt{2}-1) \sqrt{|m|} \left[1 + i \operatorname{sgn} \left(\frac{m \Delta \Omega}{\Delta W} \right) \right] \tilde{R}_m^{1/2} \right. \\ \left. + \left(\frac{53}{36} - \sqrt{2} - n^2 - k^2 r_0^2 \right) + \mathcal{O}(\tilde{R}_m^{-1/2}) \right\}, \quad (\text{A8}) \end{aligned}$$

where $\operatorname{sgn} x$ denotes the sign of x and $n = 1, 2, 3, \dots$ is the radial wavenumber. As $\eta \propto \tilde{R}_m^{-1}$, the leading-order term on the right-hand side is $\mathcal{O}(\tilde{R}_m^{-1/2})$. Note that Ruzmaikin et al. [18] use the same notation for n , but wrongly state that $n = 0$ for the first radial mode.

To the leading order in \tilde{R}_m , the magnetic field is given by

$$\hat{B}_\varphi = \exp \left[-\sqrt{2i|m|\tilde{R}_m} \frac{(r-r_0)^2}{2r_0^2} \right] + \mathcal{O}(\tilde{R}_m^{-1/2}), \quad (\text{A9})$$

$$\hat{B}_r = \sqrt{2i|m|\tilde{R}_m^{-1/2}} B_\varphi + \mathcal{O}(\tilde{R}_m^{-1}), \quad (\text{A10})$$

$$\hat{B}_z = \sqrt{2|m|} \left[\frac{r(r-r_0)}{r_0^2} - \frac{1}{\sqrt{2}} \right] B_\varphi + \mathcal{O}(\tilde{R}_m^{-1/2}). \quad (\text{A11})$$

APPENDIX B: THE ACCURACY OF THE NUMERICAL SCHEME

We assess the accuracy of our three-dimensional simulations and the implementation of the boundary conditions by comparing solutions obtained with the 3D code in the kinematic regime with those from the corresponding 1D eigenvalue problem.

The radial dependence of the (vertically averaged) magnetic energy density is shown in Fig. 12 for the high-resolution runs of Models 1a and 2a at a time when the exponential growth has well established itself. Magnetic energy concentrates in a cylindrical shell of radius r_B and of half-width δr_B , defined in Eq. (17). For Model 1a (Fig. 12a), we find $r_B = 0.48$ and $\delta r_B = 0.16$ (see also Table III). For comparison, we have overplotted the profile obtained from the one-dimensional model.

Figure 12 shows good agreement between the three-dimensional and one-dimensional simulations everywhere except close to the outer boundary. For $r \approx R_2$, the magnetic energy in the three-dimensional simulation

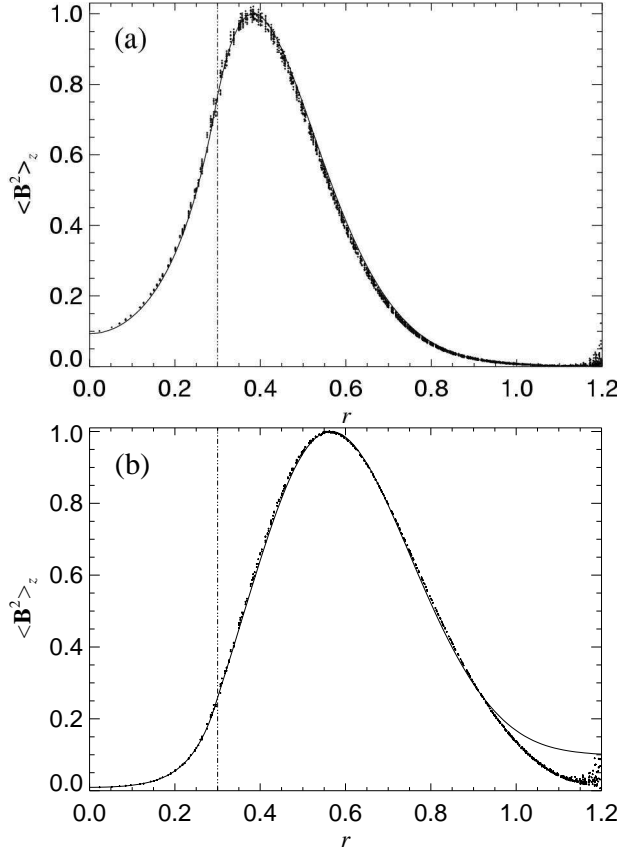


FIG. 12: The radial field structure in the kinematic regime as obtained from a three-dimensional simulation at a resolution $\delta x = 0.033$ (dots) and from solving the one-dimensional Eq. (A1) with $R_1 = 0.28$ (solid). (a) Model 1a, (b) Model 2a. Shown is the vertically averaged magnetic energy $\langle \mathbf{B}^2 \rangle_z$ in arbitrary units.

smoothly turns to zero, while in the one-dimensional calculation the tangential components of \mathbf{B} remain significant. This is due to the different boundary conditions used ($\mathbf{A} = \mathbf{0}$ vs. perfectly conducting) and the close agreement of growth rates and eigenfunctions gives us reason to believe that these are not influenced by this localized deviation.

In Table III, we compare the eigenvalues λ and the spatial parameters r_B and δr_B of the magnetic field for the three-dimensional simulations with those from the one-dimensional model for different numerical resolutions. While the high-resolution simulation has only an error of about 5% in the growth rate γ , and 0.3% in the frequency ω , the lower-resolution run yields errors of 18% and 0.9%, respectively. The main source of inaccuracy is the angular discretization of the inner cylinder boundary as illustrated in Fig. 13. If we define an effective inner radius $R_1^{(\text{eff})}$ as the radius of a circle enclosing the same area as the shaded cells in Fig. 13, then $R_1^{(\text{eff})} \approx 0.29$ for the lower-resolution run. For an inner radius of 0.29, the one-dimensional model yields a growth rate that is considerably lower and closer to what is observed in the

TABLE III: Accuracy of the three-dimensional code, illustrated for Model 1a using various resolutions δx . The effective inner radius $R_1^{(\text{eff})}$ is defined in the text. Growth rate, frequency, localization radius and width of the magnetic field distribution are given for Model 1a at different resolutions (top half). The lower half of the table shows the accurate values obtained by solving the one-dimensional problem (A1), (A2) for three different values of R_1 .

3D Model:					
δx	$R_1^{(\text{eff})}$	γ	ω	r_B	δr_B
0.067	0.291	0.0144	-1.969	0.467	0.162
0.033	0.301	0.0160	-1.957	0.478	0.160
0.017	0.300	0.0162	-1.952	0.483	0.161

1D Model:					
R_1	γ	ω	r_B	δr_B	
0.28	0.0140	-1.971	0.468	0.158	
0.29	0.0154	-1.961	0.478	0.159	
0.30	0.0167	-1.951	0.488	0.160	

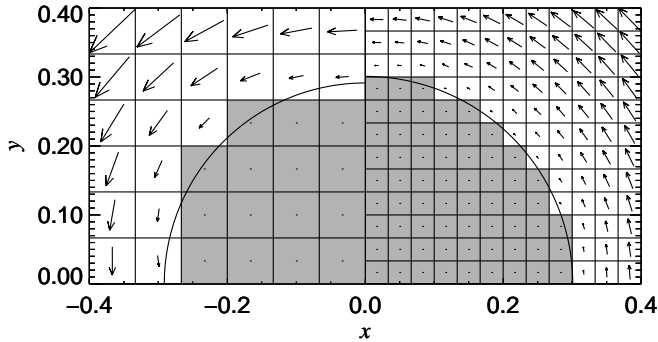


FIG. 13: The representation of the inner cylinder (shaded) on a Cartesian mesh for $\delta x = 0.067$ (left) and $\delta x = 0.033$ (right). Overlaid are the circles of effective radius $R_1^{(\text{eff})}$, and arrows representing the velocity field.

lower-resolution run (see Table III). This adjustment of $R_1^{(\text{eff})}$ results in better agreement of ω , r_b and δr_B as well.

ACKNOWLEDGMENTS

This work was partially supported by Leverhulme Trust (Grant F/125/AL) and PPARC (Grant PPA/G/S/1997/00284). Use of the PPARC supported parallel computers in St Andrews and Leicester is acknowledged.

REFERENCES

- [1] D. Lortz, *Plasma Phys.* **10**, 967 (1968).
- [2] D. Lortz, *Z. Naturforsch.* **27a**, 1350 (1972), note that this paper involves the incorrect assumption of a net axial current through the screw dynamo system, in contradiction to Cowling's theorem.
- [3] Y. B. Ponomarenko, *J. Appl. Mech. Techn. Phys.* **14**, 775 (1973).
- [4] A. Gailitis and Y. Freiberg, *Magnetohydrodynamics* **12**(2), 127 (1976).
- [5] A. Gailitis and Y. Freiberg, *Magnetohydrodynamics* **1**(1), 11 (1980).
- [6] A. Gailitis, O. Lielausis, S. Dement'ev, E. Platacis, A. Cifersons, G. Gerbeth, T. Gundrum, F. Stefanis, M. Christen, H. Hnel, et al., *Phys. Rev. Lett.* **84**, 4365 (2000).
- [7] A. Gailitis, O. Lielausis, E. Platacis, S. Dement'ev, A. Cifersons, G. Gerbeth, T. Gundrum, F. Stefanis, M. Christen, and G. Will, *Phys. Rev. Lett.* **86**, 3024 (2001).
- [8] S. A. Denisov, V. I. Noskov, D. D. Sokolov, P. G. Frick, and S. Y. Khripchenko, *Dokl. Akad. Nauk* **365**(4), 478 (1999).
- [9] P. Frick, V. Noskov, S. Denisov, S. Khripchenko, D. Sokoloff, R. Stepanov, and A. Sukhanovsky, *Magnetohydrodynamics* (2001), submitted.
- [10] A. Alemany, P. Marty, F. Plunian, and J. Soto, *J. Fluid Mech.* **403**, 263 (2000), and references therein.
- [11] F. H. Busse, U. Müller, R. Stieglitz, and A. Tilgner, *Magnetohydrodynamics* **32**(3), 235 (1996).
- [12] K.-H. Rädler, E. Apstein, M. Rheinhardt, and M. Schüller, *Studia Geoph. Geod.* **42**(3), 224 (1998).
- [13] A. Shukurov and D. D. Sokoloff, in *The Cosmic Dynamo*, edited by F. Krause et al., IAU Symp. 157 (Kluwer, 1993), pp. 367–371.
- [14] A. Königl and R. Pudritz, in *Protostars and Planets IV*, edited by V. Mannings, A. P. Boss, and S. S. Russell (Univ. Arizona Press, Tucson, 2000), pp. 759–788.
- [15] A. Ruzmaikin, D. Sokoloff, and A. Shukurov, *J. Fluid Mech.* **197**, 39 (1988).
- [16] A. D. Gilbert, *Geophys. Astrophys. Fluid Dyn.* **44**, 241 (1988).
- [17] A. D. Gilbert, Ph.D. thesis, Univ. of Cambridge (1988).
- [18] A. A. Ruzmaikin, D. D. Sokoloff, A. A. Solovyov, and A. M. Shukurov, *Magnetohydrodynamics* **25**(1), 6 (1989).
- [19] D. D. Sokoloff, A. M. Shukurov, and T. S. Shumkina, *Magnetohydrodynamics* **25**(1), 1 (1989).
- [20] E. A. Lopyan and A. Shukurov, *Magnetohydrodynamics* **3**(3), 234 (1992).
- [21] A. A. Solovyov, *Izv. Akad. Nauk SSSR. Fiz. Zemli* pp. 40–47 (1985).
- [22] A. A. Solovyov, *Izv. Akad. Nauk SSSR. Fiz. Zemli* **5**, 77 (1987).
- [23] J. Léorat, *Magnetohydrodynamics* **31**(4), 367 (1995).
- [24] A. M. Soward, *Geophys. Astrophys. Fluid Dyn.* **53**, 81 (1990).
- [25] A. D. Gilbert and Y. Ponty, *Geophys. Astrophys. Fluid Dyn.* **93**, 55 (2000).

- [26] Y. Ponty, A. D. Gilbert, and A. D. Soward, *J. Fluid Mech.* **435**, 261 (2001).
- [27] F. Krause and K.-H. Rädler, *Mean-field Magnetohydrodynamics and Dynamo Theory* (Pergamon, 1980).
- [28] Y. B. Zeldovich, A. A. Ruzmaikin, and D. D. Sokoloff, *Magnetic Fields in Astrophysics* (Gordon and Breach, N.Y., 1983), sect. 4.III.
- [29] A. P. Bassom and A. D. Gilbert, *J. Fluid Mech.* **343**, 375 (1997).
- [30] S. Chandrasekhar, *Hydrodynamic and Hydromagnetic Stability* (Dover, N.Y., 1981), §6.6.
- [31] H. Ji, J. Goodman, and A. Kageyama (2001), astro-ph/0103226.
- [32] J. Goodman and H. Ji (2001), astro-ph/0104206.
- [33] G. Rüdiger and Y. Zhang, *Astron. Astrophys.* (2001), astro-ph/0104302.
- [34] F. J. Sánchez-Salcedo and A. Brandenburg, *Mon. Not. R. Astron. Soc.* **322**, 67 (2001).
- [35] A. Brandenburg, *Astrophys. J.* **550**, 824 (2001), astro-ph/0006186.
- [36] E. G. Blackman and G. B. Field, *Astrophys. J.* **521**, 597 (1999).